ACS Applied Nano Materials, Volume 5, Issue 3, March 2022, pp. 3878-3888
DOI: 10.1021/acsanm.1c04491

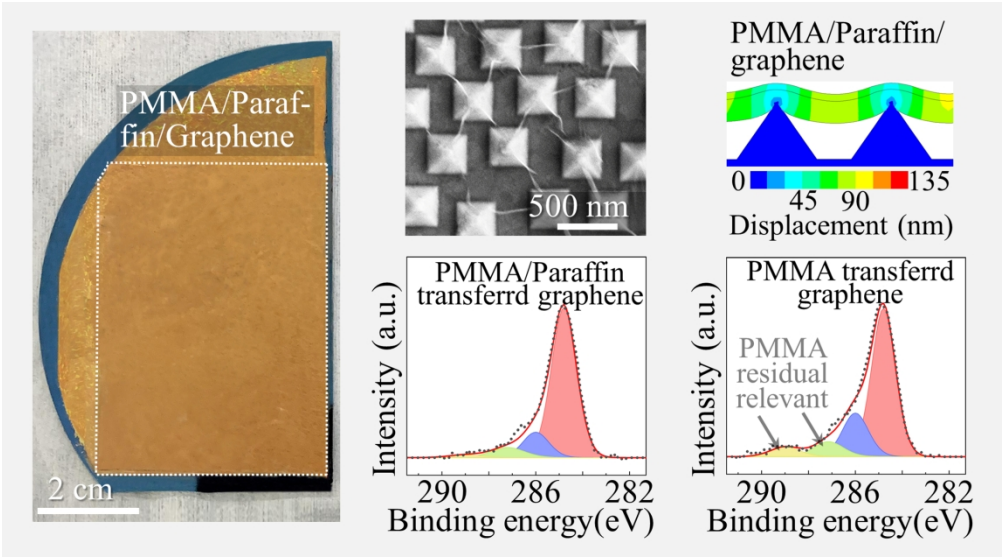

TOC Figure

68x37mm (900 x 900 DPI)

Published by ACS. This is the Author Accepted Manuscript issued with: Creative Commons Attribution Non-Commercial License (CC:BY:NC 4.0).
The final published version (version of record) is available online at DOI:10.1021/acsanm.1c04491. Please refer to any applicable publisher terms of use.

Large-Area and Clean Graphene Transfer on Au Nanopyramid-Structured Substrates: Implications for SERS Detection

*Heping Wu[1], Gang Niu[1,] *, Wei Ren[1,] *, Zhugen Yang[2], Qihang Xu[2], Liyan Dai[1], Luyue Jiang[1], Shijie Zhai[1], Jinyan Zhao[1], Nan Zhang[1], Libo Zhao[3,4], Zhuangde Jiang[4], Gang Zhao[5]*

[1] Electronic Materials Research Laboratory, Key Laboratory of the Ministry of Education & International Center for Dielectric Research, School of Electronic Science and Engineering & The International Joint Laboratory for Micro/Nano Manufacturing and Measurement Technology, Xi'an Jiaotong University, Xi'an 710049, China

[2] Cranfield Water Science Institute, School of Water, Energy and Environment, Cranfield University, Cranfield, MK43 0AL, UK

[3] School of Mechanical Engineering, Xi'an Jiaotong University, Xi'an 710049, China

[4] The State Key Laboratory for Manufacturing Systems Engineering & The International Joint Laboratory for Micro/Nano Manufacturing and Measurement Technology, Xi'an Jiaotong University, Xi'an 710049, China

[5] The college of Life Sciences and Medicine, Northwest University, No. 229 Taibai North Road, Xi'an, Shaanxi, 710069, P.R. China

Keywords: graphene transfer, PMMA/paraffin, Au nanopyramid, Raman spectroscopy, polarization-dependent, tensile strain

ABSTRACT. The transfer of large-area and clean graphene to arbitrary substrates, especially to those with raised nanostructures represents a great challenge. Polymer-based supporting layers generally lead to organic residues while graphene transfer using alternative supporting materials like paraffin suffers from breaking and thus limits the transfer area. We demonstrated an improved PMMA/paraffin double-layer enabling the large-area transfer of graphene with high cleanliness and high coverage (81%) onto Au nanopyramids (AuNPs) structured substrates. The impact of supporting layers including single PMMA or paraffin and mixed PMMA/paraffin was clarified. The properties of graphene on AuNPs were theoretically and experimentally examined

in detail. Raman spectra show a polarization-dependent D peak due to the folding of large-curvature graphene. The graphene on AuNPs shows a slightly tensile strain and provides an extra surface-enhanced Raman scattering (SERS) with an enhancement factor of ~20 times. These findings open a pathway to extend the applications of transferred graphene on raised nanostructures in many fields, such as SERS detection, catalysis, biosensors, light-emitting diodes, solar cells, and advanced transparent conductors.

1. Introduction

Since its discovery in 2004, graphene has attracted enormous interest because of its unique properties including high electron mobility, high thermal conductivity, optical transparency and flexibility.[1] This makes graphene promising for various applications, not only for semiconductor microchips, sensors and batteries, but also for medical and flexible wearable devices.[2-3] Large-size and high-quality graphene monolayers are indispensable for all applications. Therefore, significant efforts have been made for graphene growth. The most common and efficient way is to grow graphene using chemical vapor deposition (CVD) method at high temperatures on metal foils, such as Cu, Ni, Co, Ir, Ru, Pd, Pt, etc.[4-5] The carbon source (e.g., methane) generates active

carbon atoms at high temperatures, which dissolve in the metal surface and precipitate out during the subsequent cooling process, forming graphene. Furthermore, the metal substrate also serves as the catalyst to reduce the reaction temperature.[6] The low solubility of carbon in Cu helps make the growth process self-limiting on its surface,[5] which makes Cu an excellent substrate for growing single-layer, uniform-thickness (95%) and large-area graphene films. Furthermore, graphene growth on important dielectric substrates such as SiO_2, $SrTiO_3$, *etc.*, and semiconductors such as Si, Ge, *etc.*, by special CVD methods (including atmospheric pressure CVD, plasma-enhanced CVD, *etc.*) have also been reported.[7] In general, the growth of high-quality and large-area uniform graphene on Cu substrates is the most mature.[5, 8-10]

The transfer of graphene from Cu foils to the targeting substrate while maintaining its high quality is another significant issue that limits graphene application. Graphene monolayer is thermodynamically unstable and cannot exist in the free-standing state,[11-12] thus supporting layers are indispensable. Polymers like polymethyl methacrylate (PMMA) and polydimethylsiloxane (PDMS) are widely accepted as the supporting layers, which allow the large size and flat graphene transfer.[13] However, such transferred graphene suffers from organic residue contaminations due to the difficulty in completely removing the polymers, which

degrades the quality of the graphene. Recently paraffin was proposed as an alternative supporting material,[14] which leads to clean graphene transfer but its application for large-area graphene transfer is not yet demonstrated. On the other hand, the targeting substrate also strongly impacts the graphene quality. For example, Si wafer with silica layer is the most widely used targeting substrate.[5, 14-16] Experimental evidence and theoretical analysis both reveal that electrical charges at the SiO_2 surface originating from both the oxide fabrication process and protonation reactions lead to high interaction between graphene and SiO_2.[17-18] Moreover, many applications like surface-enhanced Raman scattering (SERS),[19] biosensors,[20] catalysis,[21] as well as novel graphene-based optoelectronic devices such as light-emitting diodes,[22] solar cells,[23] or advanced transparent conductors require high-quality graphene on nanostructures.[24-25] For instance, graphene on Au nanopyramids (AuNPs) greatly enhances the SERS capability, as well as protects the metallic structure from oxidation.[26] The nanostructured substrates alter the graphene morphology and possibly lead to defects. The small contact area between graphene and nanostructures results in poor adhesion of graphene to the nanostructured substrate, further causing graphene wrinkles and breakages. The detailed study of graphene properties on nanostructured substrates is still lacking.

In this work, we transfer graphene using the wet process from Cu to nanostructured AuNP substrates using different supporting materials. The proposed PMMA/paraffin bilayers lead to large-size and clean graphene transfer, thanks to the combination of chemical stability of paraffin and large tensile strength and high Young's modulus of PMMA. The properties including defects, strain and doping of graphene on AuNP substrate were experimentally and theoretically studied in detail. The impact of the AuNP pattern on the graphene property was also examined. These results are certainly of great interest in further enabling the large-area and high-quality graphene transfer for various applications.

2. Experimental Section

2.1. Au pyramidal substrate fabrication. The substrates of raised AuNPs with different sizes were fabricated by a template printing and epoxy-enabled transfer process of the Au layer. The Au layer was firstly deposited by magnetron sputtering on a Si mold with periodic inverted nano-scale pyramidal pits, and then was peeled off and transferred to a new substrate, with the raised AuNPs outward. The Si mold with pyramidal holes was fabricated by colloidal lithography combined with modern semiconductor nanofabrication process. Firstly, a monolayer colloidal crystal of polystyrene (PS) microspheres with different diameters (500 nm, 350 nm, 200 nm)

were prepared on the SiO_2/Si wafer using the Langmuir-Blodgett method.[27] Dry-etched PS microspheres with reduced diameters serve as the template, followed by the deposition of a chromium layer. After lifting off the PS layer, the Cr holes serve as the etching mask for dry-etching SiO_2 layers. Then periodic reversed Si pyramidal pits were created by anisotropic etching in KOH solutions since KOH preferentially etches Si along the (001) plane. More detailed fabrication processes were shown in SI (Figures S3 to S5).

2.2. PMMA-supported graphene transfer. PMMA solution (6% wt) was spin-coated onto the commercial CVD graphene (Wuxi Huicheng Graphene Tech&Appl Co., Ltd., CVD growth on copper foil) at a speed of 500 rounds per minute (rpm) for 10 seconds (s) and followed by a spin at a speed of 1500 rpm for 40 s, then being dried at room temperature for 10 minutes (min). The thickness of the fully dried PMMA layer was about 300 nm. After that, the graphene layer grown on the back-side of the Cu foil was removed by treating for 5 min in the UV-ozone. Then the Cu foil was etched by floating the PMMA/graphene/Cu stack on the surface of $FeCl_3$ solution (1M) for 30 min. The PMMA-supported graphene film was then rinsed with deionized (DI) water several times. Subsequently, the destination substrate was contacted with the PMMA-supported graphene layer and the sample was initially dried in the air, followed by an oven baking at 80 ˚C

for 5 hours (h). The sample was soaked in acetone at 60 ˚C for 1 h to remove the PMMA layer. The sample was then rinsed with isopropanol (IPA) and dried in the air, leaving the graphene monolayer on the targeting substrate.

2.3. Paraffin-supported graphene transfer. The paraffin (Sigma-Aldrich) with a melting point at around 50~60 ˚C was melted in an oven at 80 ˚C before being used. Keeping the molten state by a heating gun, paraffin was spin-coated onto the graphene/Cu foil at a speed of 700 rpm for 90 s, followed by removal of the backside graphene and the etching of the Cu foil. After multiple times rinsed in DI water, the paraffin/graphene stack was then transferred onto 40 ˚C deionized water and kept at the same temperature for 2 h, where the paraffin layer remained at a solid-state. Subsequently, the paraffin-supported graphene was scooped up to the targeting substrate and was dried in the air, followed by an oven baking at 40 ˚C for 5 h. Finally, the sample was soaked in hexane at 60 ˚C for 1 h to remove paraffin, followed by being rinsed in clean hexane for 10 min. The sample was dried in the air.

2.4. PMMA/Paraffin double-layer supported graphene transfer. PMMA/paraffin-supported graphene was used to protect the paraffin/graphene stack from breaking during the transferring process. After the paraffin layer was solidified, PMMA was spin-coated on the paraffin layer

123 with the same parameters as those used in the PMMA-supported transfer method. The following
124 procedures were mostly the same as the paraffin-supported transfer method except removing the
125 PMMA layer in acetone for 10 min before soaking the sample in hexane at 60 ˚C.

126 **2.5. Characterization method.** The surface morphology characterization was carried out using an
127 optical microscope (OM, OLYMPUS BX51-P), scanning electron microscopes (SEM, FEI
128 Quanta FEG 250 and ZEISS GeminiSEM 500), and an atomic force microscope (AFM) system
129 (Dimension Icon, Bruker). The acceleration voltage of SEM is 10 kV. X-ray photoelectron
130 spectroscopy (XPS) test was performed using a Kratos Axis Ultra DLD system (Al target). The
131 coverage of transferred graphene was estimated using software Image J.

132 The Raman spectra of graphene were obtained using a Horiba LabRAM HR Evolution Raman
133 spectrometer under ambient conditions. The excitation laser wavelength was 633 nm with the
134 power being kept at 1.75 mW for a single spectrum and at 0.7 mW for areal mapping spectra.
135 The grating was 600 lines/mm and the spectroscope was equipped with a high speed encoded
136 stage that could move in x, y, and z directions and had a 100 nm step spatial resolution. The
137 polarized Raman spectrum of graphene was obtained using a Renishaw inVia Qontor. The
138 Raman spectra in the paper are the average spectra of multi-acquisitions and baseline corrected.

2.6. Finite element simulation of the deformation. Finite element simulation was performed using the software Ansys to calculate the temperature field and deformations of the different types of supporting layer and graphene stacks. The constructed models are composed of 3 nanopyramids with different supporting layer/graphene stacks. The thickness of graphene is 0.335 nm.[28] The minimum mesh size of the support layer and graphene layer is 5 nm. The heat treatment during the transfer process was simulated by applying a thermal load at the bottom of the models. Then the obtained temperature field as well as a simulated gravity load were applied to calculate the structural deformation. The element type for thermal calculation is plane 55, and for structural calculation is plane 182.

3. Results and Discussion

3.1. The impact of supporting layers for graphene transfer.

Graphene monolayers on Cu foils were transferred on AuNP nanostructured substrates. PMMA, paraffin and PMMA/paraffin layers were employed as the supporting layers in the wet transfer process. It is noted there that compared to the dry transfer process, the wet transfer is better to protect the nanostructures because it is free from high pressure or temperature

154 treatment.[29] **Figure** 1a shows the wet transfer process. The supporting layer was spin-coated on
155 the CVD-grown graphene on the Cu foil. The Cu substrate was then etched by the $FeCl_3$
156 solution, and the sample was subsequently scooping-transferred into deionized (DI) water 3
157 times to remove the Cu etcher. After the supporting layer/graphene stack was transferred to the
158 pyramidal substrate and dried, the supporting layer was removed by chemical solvent. Figures 1b
159 ~ 1d show the photos of different supporting layers/graphene stacks floating on the DI water. It
160 can be observed that graphene supported by different layers shows different morphology.
161 Different from PMMA (Figure 1b), which leads to large-size and complete graphene transfer,
162 paraffin supporting layer (Figure 1c) results in a high possibility of breaking for large size
163 samples, although it permits the complete transfer of smaller size graphene (Figure 1c inset).
164 Using the combined bi-layer PMMA/paraffin supporting layer (Figure 1d), one can obtain large-
165 size and complete graphene transfer. The paraffin layer shows a distinct size effect when being
166 used as a graphene-transferred supporting layer. As shown in Figure 1e, both the sample size and
167 the paraffin thickness impact the intact possibility of the paraffin/graphene stack. Thinner
168 paraffin wax thickness or larger size of the transferred graphene both easily cause the
169 paraffin/graphene stack breaking during the transfer process, which greatly limits the efficiency

of graphene transfer using paraffin as a supporting layer. The thicknesses of the paraffin layer at different centrifugal speeds are shown in Figure S7. Spin-coating a layer of PMMA on the surface of paraffin significantly prevents the paraffin/graphene stack from breaking and realizes graphene transfer at a large scale, which benefits from higher tensile strength and young's modulus of PMMA of 70 MPa and 1800 MPa, respectively, those of which for paraffin are 0.885 MPa and 192 MPa, respectively. More details can be found in Table 1. Figure 1f shows the chemical structures, formulae, and ball-and-stick models of an MMA (monomer of PMMA) dimer and a paraffin molecule. It can be seen that PMMA has the chemically active group of the carbonyl group (C=O) whereas paraffin molecule is chemically stable and unreactive as a saturated alkane structure. The stable chemical properties of paraffin lead to clean graphene transfer, while the PMMA/paraffin double-layer structure can facilitate large-area graphene transfer.

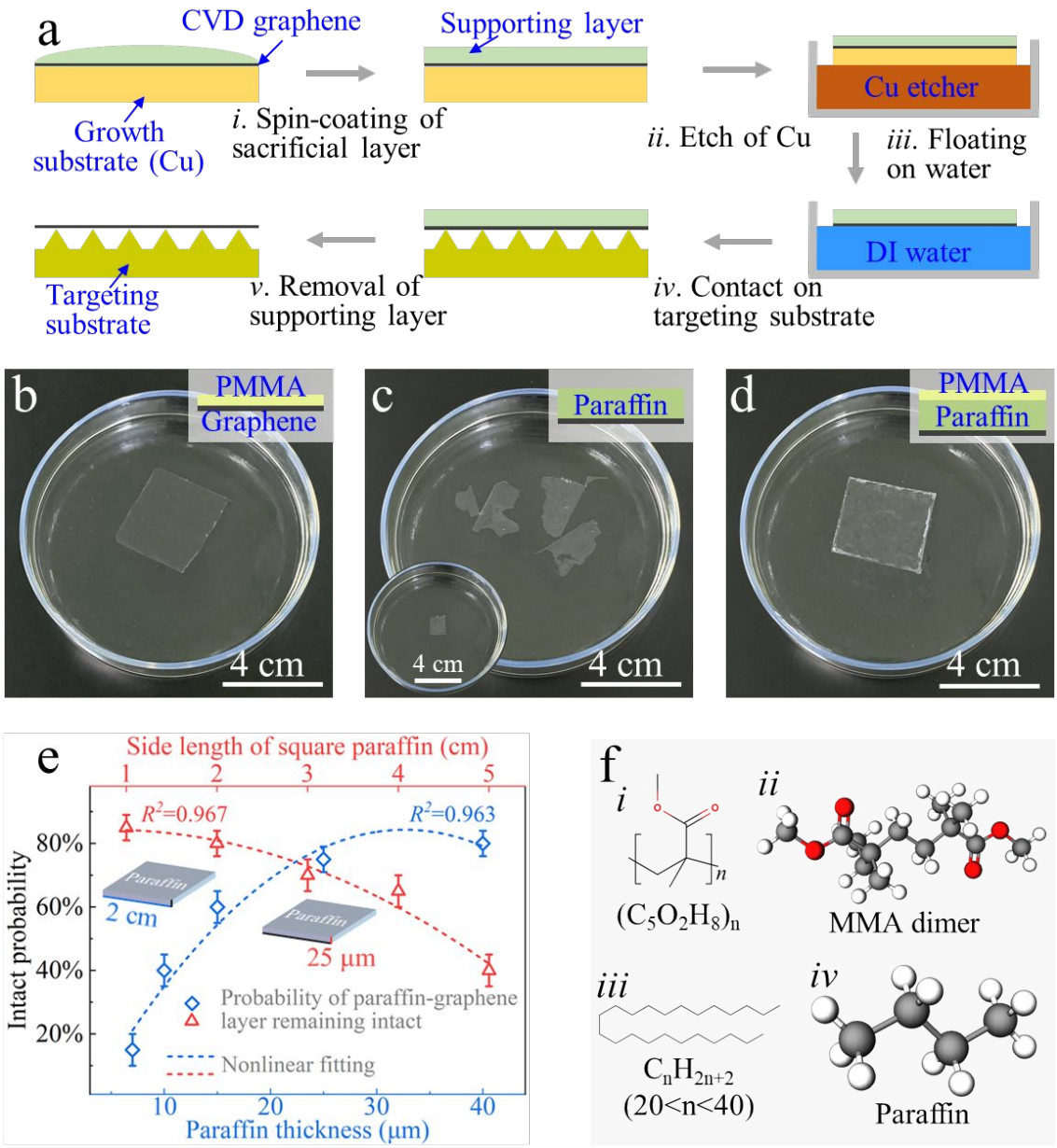

182

183 **Figure 1.** (a) Schematic illustration of the wet transfer process of graphene. Photos of different

184 supporting layers with graphene floating on water, (b) PMMA/graphene, (c) paraffin/graphene,

185 (d)PMMA/paraffin/graphene. (e) Size-effect of pure paraffin layer as a supporting layer. When

186 studying the impact of the other parameter, the thickness and side length of the square paraffin

187 stacks were fixed to 25 μm and 2 cm, respectively. (f) Chemical structures, formulae, and ball-
188 and-stick models of a PMMA dimer and a paraffin molecule. Chemical structures and formulae
189 of (*i*) PMMA and (*iii*) paraffin, and the ball-and-stick models for (*ii*) an MMA dimer and (*iv*) a
190 paraffin molecule. Carbon atoms are in gray, hydrogen atoms are in white, oxygen atoms are in
191 red.

192 **3.2. Cleanliness of graphene transferred by different supporting layers.**

193 The residual polymer contamination during the transfer would severely impact the quality
194 of graphene and the supporting layer plays an important role in this process. To examine the
195 cleanliness of graphene transferred by different supporting layers, PMMA, paraffin and
196 PMMA/paraffin layers were used. Flat Au/Si substrates were used here for the convenience of
197 the morphology and chemistry studies and the results can be transplanted to graphene transferred
198 on other substrates including nanostructured substrates. **Figures 2** show the scanning electron
199 microscopy (SEM) (Figures 2b ~ 2d) and atomic force microscopy (AFM) (Figures 2f ~ 2h)
200 characterizations as well as X-ray photoelectron spectroscopy (XPS) analyses (Figures 2j ~ 2l) of
201 transferred graphene on Au films using different supporting layers. Figure 2a shows the SEM
202 image of bare Au film before graphene is transferred. It can be seen from Figure 2b that PMMA

residues (white spots marked by green arrows) exist on PMMA-transferred graphene.[15] Some wrinkles of graphene can also be observed, which were marked by blue arrows. Graphene monolayers transferred by paraffin (Figure 2c) and PMMA/paraffin double layer (Figure 2d) are relatively clean, with no observable organic residues and fewer wrinkles (blue arrows). The AFM results of the transferred graphene confirm the SEM observation. The root mean square (RMS) roughness of paraffin (Figure 2g) and PMMA/paraffin (Figure 2h) transferred graphene are 2.6 nm and 2.7 nm, respectively, which are very close to that (2.4 nm) of primitive Au film (Figure 2e) and are both smaller than that (3.2 nm) of PMMA transferred graphene (Figure 2f). XPS characteristics of C1s peak reveal more details. It can be seen that the C 1s peak of graphene on Cu before the transfer (Figure 2i) can be fitted by two components at 284.8 eV and 285.9 eV, corresponding to C=C (red) and C–OH bonds (blue), respectively. For PMMA transferred graphene (Figure 2j), in addition to the graphene bonds, two additional components appear at 287.2 eV and 289.0 eV, corresponding to C=O (green) and O=C–OH (yellow) bonds arising from the residual PMMA during the Cu etching step.[30] The paraffin and PMMA/paraffin-transferred graphene also show these two components but with much lower intensities, as shown in Figure 2k and Figure 2l, respectively. More OM images were shown in Figure S1. The cleaner

surface with fewer wrinkles of graphene transferred by paraffin and PMMA/paraffin benefit from the stable chemical properties and high thermal expansion coefficient of paraffin.[14] It is worth noting here that graphene transferred to flat Au films using the three types of supporting layers all show high transfer rates of over 90%.

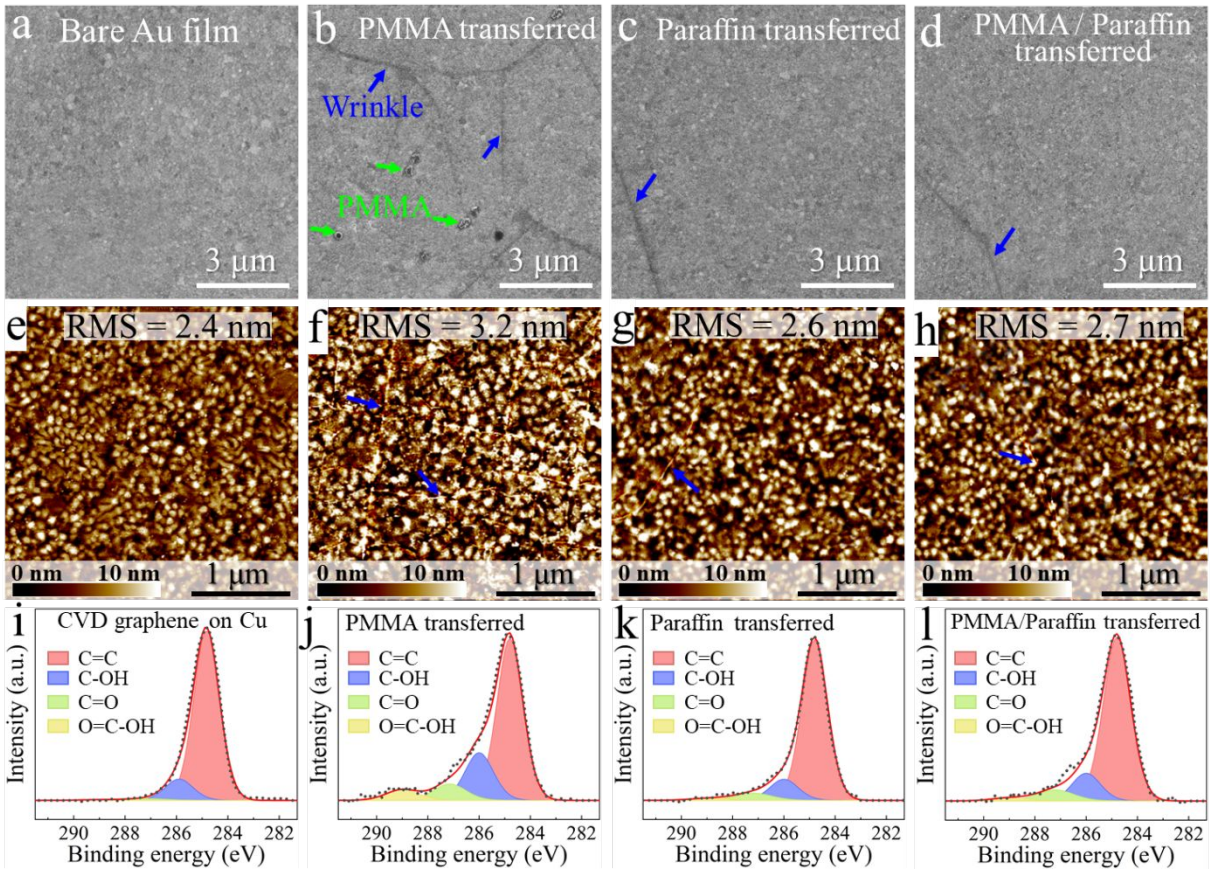

Figure 2. (a) and (e) Surface morphologies (SEM and AFM) characterization of the bare Au film. (i) XPS analysis of pristine CVD graphene on Cu foil. Surface morphologies (SEM and AFM) characterization and XPS analyzes of graphene on the Au films transferred by different

supporting layers, (b), (f) and (j) PMMA, (c), (g) and (k) paraffin, (d), (h) and (l) PMMA/paraffin double layer.

3.3. Graphene transferred to AuNPs structured substrate using different supporting layers

When transferring graphene on nanostructured substrates, particularly with uneven structures like AuNPs, one faces more challenges maintaining the intactness and high quality of the graphene layer. Here we examine the graphene properties transferred on highly uniform wafer-scale Si substrate with raised periodical AuNPs, which is widely used for biosensors or optoelectronics applications.[19] Figures 3 show OM images of the AuNPs substrate without graphene (Figure 3a) and with graphene transferred by PMMA (Figure 3b), paraffin (Figure 3c) and PMMA/paraffin double layer (Figure 3d). The bare AuNPs substrate shows a homogeneous pink surface. For graphene-covered substrates, regions covered by graphene monolayer exhibit gray color, while regions with obvious wrinkles show a darker gray color. SEM images of bare AuNPs (Figure 3e) and graphene-covered AuNPs (Figure 3f) show more details of the morphology. The nanopyramids have bottom side lengths of ~330 nm and gap distances between two pyramids of ~170 nm. Substrates with these sizes are marked as substrate #1 in the following, distinguishing them from other substrates with different AuNP patterns. The angle

243 between the inclined surface and the bottom of the pyramid is 54.74˚, which is determined by the
244 anisotropic etching of the Si (001) plane. The bottom between nanopyramids is connected by the
245 Au film. The blue arrow in Figure 3f marks a graphene wrinkle between two nanopyramids.
246 Raman spectra were studied to explore the graphene properties, as shown in Figure 3g. It can be
247 seen that graphene on AuNPs (blue and yellow curves) shows much stronger G (at 1586 cm^{-1})
248 and 2D peaks (at 2640 cm^{-1}) compared to those of graphene on the flat Au film (black curve),
249 due to the SERS effect (will be discussed in detail in Section 3.6).[31] Comparing the spectrum
250 collected at graphene flat regions (orange) with that collected on a wrinkle (blue), it can be seen
251 that the ratio of G/2D grows as a result of the presence of double or multilayer graphene in
252 wrinkles, as observed in the literature.[5] The thickness of transferred graphene monolayer is 1.1
253 nm (Figure S2).

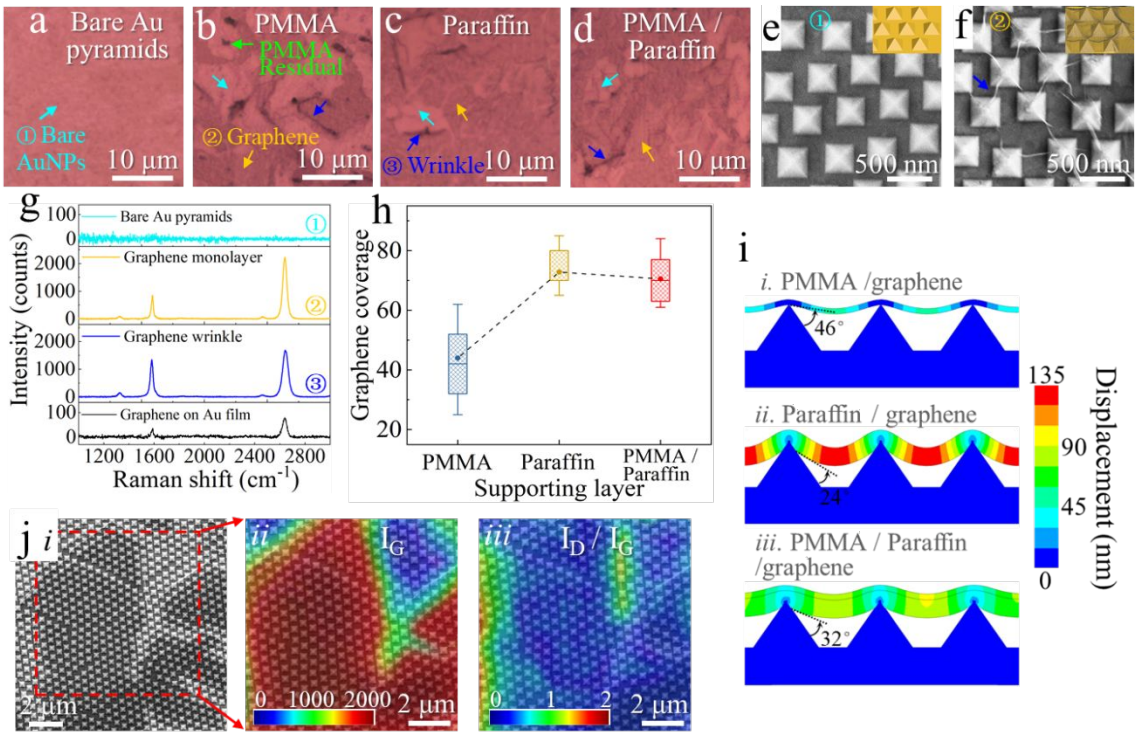

254

255 **Figure 3.** Graphene transfer to the AuNPs substrate. OM characterization of AuNPs substrates

256 (a) without graphene and with graphene transferred by (b) PMMA, (c) paraffin, (d)

257 PMMA/paraffin. SEM morphologies of the AuNPs (e) before and (f) after graphene transferred

258 on the surfaces. PMMA residual is in green arrow, graphene monolayer is in orange arrow,

259 graphene wrinkle is in blue arrow, and bare AuNPs are in cyan arrow. (g) Raman spectra of

260 graphene at different regions corresponded to Figures 3a ~ 3d. (h) Coverage of transferred

261 graphene on substrate #1 by different supporting layers. (i) Finite element simulation results of

262 graphene transfer to nanopyramidal substrates using different types of supporting layers: (*i*)

263 PMMA, (*ii*) paraffin, (*iii*) PMMA/paraffin. (j) SEM image of the AuNP substrate and Raman
264 mappings of (*ii*) G peak intensity and (*iii*) I_D/I_G of graphene superimposed on the SEM image.

265 Based on the contrast difference in OM images shown in Figure 3b-d, the graphene
266 coverage was estimated using software Image J (Figure S8), and the results were shown in
267 Figure 3h. It is noted here that the estimated coverage value is an average value from multiple
268 experiments including more than 30 times transfer process and the total transferred graphene
269 area of each method is more than 120 cm^2. PMMA-transfer method (blue) shows a lowest
270 average coverage of ~44%, while paraffin (yellow) and PMMA/paraffin (red) transfer method
271 show similar higher average coverages of ~70%. Smaller boxes for paraffin and PMMA/paraffin
272 transfer methods indicate their transfer coverages are more stable. Finite element simulation was
273 performed to further theoretically understand such differences and the results were shown in
274 Figure 3i. The displacements of PMMA/graphene, paraffin/graphene and
275 PMMA/paraffin/graphene after a heating treatment were shown in Figures 3i-*i*, 3i-*ii* and 3i-*iii*.
276 Owing to the significant differences between mechanical properties of PMMA and paraffin (the
277 tensile strength and Young's modulus, are 70MPa and 1800 MPa respectively for PMMA
278 whereas being 0.885 MPa and 192 MPa for paraffin), the contact area of the hybrid graphene

279 stack with the nanopyramids shows a maximum (46˚) and minimum (24˚) value of the contract
280 angle (the angle between graphene and the nanopyramid slope) when using pure PMMA and
281 paraffin, corresponding to the minimum and maximum coverage, respectively. Graphene
282 supported by PMMA/paraffin double layer has a medium value (32˚) of the contact angle. The
283 contact area between graphene transferred by paraffin as well as PMMA/paraffin and
284 nanopyramids are much larger than the area of PMMA-transferred graphene, leading to higher
285 transfer coverages. The material properties used for finite element simulation are shown in Table
286 1.

287 The graphene property, particularly the defected regions was further studied by Raman spatial
288 mapping, as shown in Figure 3j, superimposed on the SEM images. Figure 3j-*i* shows the SEM
289 morphology of a graphene fragment on the pyramidal substrate. Raman mapping was performed
290 on the area within the red dashed box. Figures 3j-*ii* and 3j-*iii* show the Raman mapping of G
291 peak intensity and the ratio of D peak intensity and G peak intensity (I_D/I_G). The G peak intensity
292 mapping well demonstrated the graphene location on the nanopyramidal substrate, which agrees
293 well with the SEM image. Graphene shows a slightly defected structure in many regions (blue
294 part), revealed by the low value of D peak intensity. At the two edges of the graphene fragment,
295 the D peak intensity is significantly higher, because the graphene edges act as defects.[32]

296 **Table 1.** The material properties used for finite element simulation

Physical property	Unit	PMMA[33-34]	Paraffin [14, 35-36]	Graphene [37-39]	Au [40]
Young's modulus	MPa	1800	192	1E6	7.8E4
Tensile strength	MPa	70	0.885	1.3E5	80
Linear expansion coefficient	K^{-1}	7E-4	1.6E-3	-5E-5	1.4E-5
Density	kg/m^3	1100	900	2267	1.9E4
Specific heat capacity	J/kg K	1466	2140	700	130
Thermal conductivity	w/m K	0.19	0.24	600	300
Poisson's ratio	1	0.35	0.37	0.2	0.42

297

298 **3.4. Electronic properties of graphene: D peak discussion**

299 To understand more about the electronic structure of the graphene monolayer on AuNPs,
300 the polarization dependence of the Raman D peak of graphene was studied. It is widely accepted
301 that the D peak originating from the defects of graphene is mainly located on the edges and
302 cracks and it was theoretically predicted that large curvature folds in graphene will lead to
303 polarization-dependent D peaks.[41] The graphene fold between two nanopyramids is an ideal
304 large-curvature graphene fold for study, as shown in **Figure 4a** by an SEM photo. Figure 4b
305 shows that the intensities of D peak (at 1322 cm^{-1}) and D' peak (at 1619 cm^{-1}) change obviously
306 as the polarization angle varies from 0˚ (blue) to 90˚(red) then to 180˚ (green) and finally to 270˚

(black), while the intensities of G peak (at 1585 cm^{-1}) and 2D peak (at 2637 cm^{-1}) do not change at all. Such dependence of the D peak on the polarization angle was illustrated more clearly in Figure 4c, by the $\cos^2\theta$ fitting of the intensity variation of the D peak as a function of the polarization angle.[42] Moreover, the dependence of I_D/I_G, G peak and 2D peak was examined and shown in Figure 4d under polar coordinates. In contrast to the polarization irrelevance of the intensities of G peak (black triangles) and 2D peak (green rhombus), the intensity of I_D/I_G exhibits an obvious polarization correlation with 2-fold symmetry. The graphene fold provides ideal specular scattering in two dimensions, forming the double-resonant D peak.[41] Similar phenomena were also observed in the literature.[43] As a comparison, the polarization Raman test was also performed at the area without large-curvature graphene fold, and the D peak of graphene does not show polarization dependence, as shown in Figure S9.

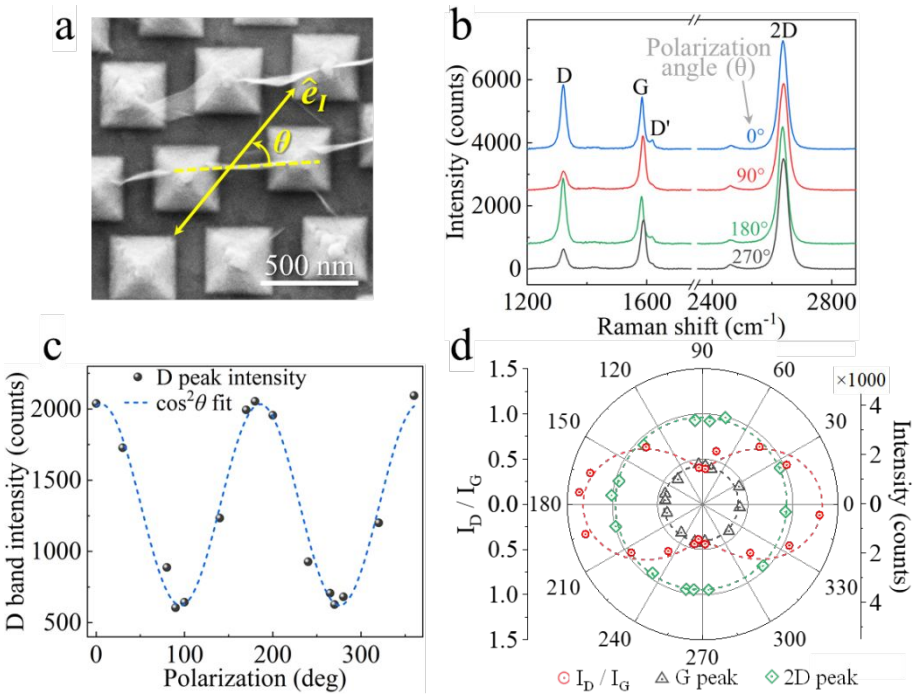

Figure 4. The polarization dependence of D peak generated by graphene folds on the direction of incident light. (a) SEM characterization of parallel graphene wrinkles. The yellow line shows the polarization direction of the incident light $\hat{e}_I$, and the dotted line shows the direction of graphene fold, the angle between which is θ. (b) The Raman spectrum of graphene fold under different polarization angles. (c) The $\cos^2\theta$ fitting of the intensity of D peak with the polarization angle. The black dots are the experimental measurements, and the blue line is the fitted curve. (d) The polar coordinate fitting of Raman intensities of G peak, 2D peak and I_D/I_G of graphene fold as functions of the polarization angle. The corresponding experimental measurements are

represented by black triangles, green diamonds and red circles. The fitted curves are represented by black, green and red dashed lines, respectively.

3.5. Strain, doping and nanometer-scale strain variations analysis.

To further understand the strain and doping status of the graphene on AuNPs substrates, the Raman spectra were analyzed in more detail. **Figure 5** summarizes the extracted information about strain, doping and nanometer-scale strain variations by showing the scatter plots of ω_{2D} and ω_G obtained from a series of Raman spectra (in total 100 positions) measured from an area of 50 × 50 μm^2. The full-width-at-half-maximum (FWHM) of the 2D peak, Γ_{2D}, is related to the graphene homogeneity as well as the amount of nanometer-scale strain variations in the graphene lattice.[44] Γ_{2D} information was color-coded in the data points in Figures 6a ~ 6c. It is observed that graphene transferred by PMMA (Figure 6a) shows larger values of Γ_{2D} whereas graphene transferred by paraffin (Figure 6b) and PMMA/paraffin (Figure 6c) mainly show low nanometer-scale strain variations and non-homogeneity as seen by the smaller values of Γ_{2D} (cyan and blue color of data points). This can be attributed to the impurity of PMMA residues on graphene transferred by PMMA.

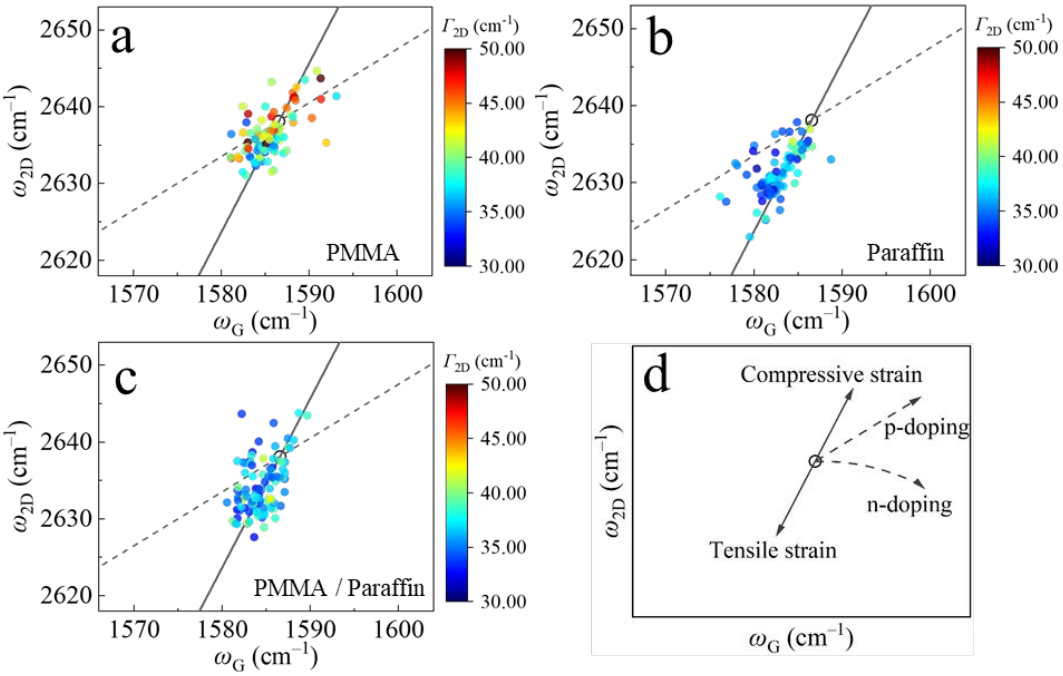

342

343 **Figure 5.** Scatter plots of ω_{2D} versus ω_G extracted from the spatially resolved Raman spectra

344 recorded of substrate #1 with graphene transferred by (a) PMMA, (b) paraffin, and (c)

345 PMMA/paraffin. (d) Schematic representation of the influence of strain, p- and n-doping on ω_{2D}

346 and ω_G. The black dashed lines correspond to the doping axes and the solid black lines

347 correspond to the strain axes. The black circles represent the point of pristine unstrained

348 graphene.

349 To further compare the strain and doping in graphene transferred to nanopyramidal

350 substrates and flat Au film, we employ a 'vector' decomposition model on the position of the G

351 peak and the 2D peak.[45] Figure 5d shows a schematic illustration of the influence of strain,

352 doping of the graphene on its Raman spectrum. Strain and doping of the graphene have been
353 extracted into vectors with different relative slopes of 2.2 for pure strain effect (solid black lines
354 in Figure 5), 0.7 for hole doping effect (straight black dashed lines), and a nonlinear decrease of
355 n-doping (curve black dashed lines).[46] Strain and doping of graphene transferred to flat Au film
356 by paraffin is taken as zero strain and zero doping point, marked by the black circle. Former
357 research has proved that strain and doping of paraffin-transferred graphene approach that of
358 intrinsic graphene well.[14] According to the above analysis, graphene transferred to nanopyramids
359 overall show tensile strain, which shows a maximum value in the paraffin-transferred graphene
360 (Figure 5b). PMMA/paraffin double layer (Figure 5c) and PMMA (Figure 5a) transferred
361 graphene show decreasing tensile strain, which is especially nearly zero for PMMA transferred
362 graphene. Transferred CVD graphene usually exhibits a compressive strain, which originates
363 from the growth technics and negative thermal expansivity.[47] While for AuNP substrates with
364 raised nanostructures, the compressive strain is released at the valley area among the raised
365 structures after the supporting layer is removed. The tensile stress is generated when the
366 supporting layer/graphene stack conformally adheres to the AuNPs surface, and the magnitude of
367 the tensile stress is positively related to the degree of conformal physisorption.[48] The tensile

368 stress is then enlarged by the formation of graphene wrinkles after the supporting layer is
369 removed. The paraffin transferred and PMMA transferred graphene has the smallest and the
370 largest contact angles with the pyramid slope, respectively (see Figure 3i). Therefore, they show
371 the largest and the smallest tensile stress, respectively.

372 **3.6. Nanopyramid density impact and SERS effect.**

373 To study the impact of the nanopyramid density on the graphene transfer coverage,
374 substrates with denser nanopyramids (compared to substrate #1) were fabricated, as shown in
375 Figures 6a (substrate #2) and 6d (substrate #3). Figures 6b and 6c, 6e and 6f show the SEM and
376 OM images of the corresponding substrate after transferring graphene by PMMA/paraffin. The
377 molds of samples #2 and #3 were fabricated using PS microspheres with diameters of 350 nm
378 and 200 nm, respectively. The prepared nanopyramids with different densities (4, 8 and 25
379 nanopyramids per μm^2 for substrate #1, #2 and #3, respectively) have the same ratio of 1.9 of
380 bottom side length to distance between two pyramids, as shown in Figure S6. Figure 6g shows
381 the graphene coverage of substrates with different nanopyramid densities. Graphene coverage
382 increases as the density of the nanopyramids augment, and the average coverages rise to 77%
383 and 81% for AuNP substrate #2 and #3, respectively. The finite element simulation (Figure 6h)

shows that the contact area between a single nanopyramid and transferred graphene decreases as the density of nanopyrmaid increases. The contact angles between the graphene and the nanopyramid change from 32˚ for substrate #1 (Figure 3i-*iii*) to 34˚ for substrate #2 and to 38˚ for substrate #3. The increase of graphene coverage could attribute to a larger total contact area between graphene and AuNPs.

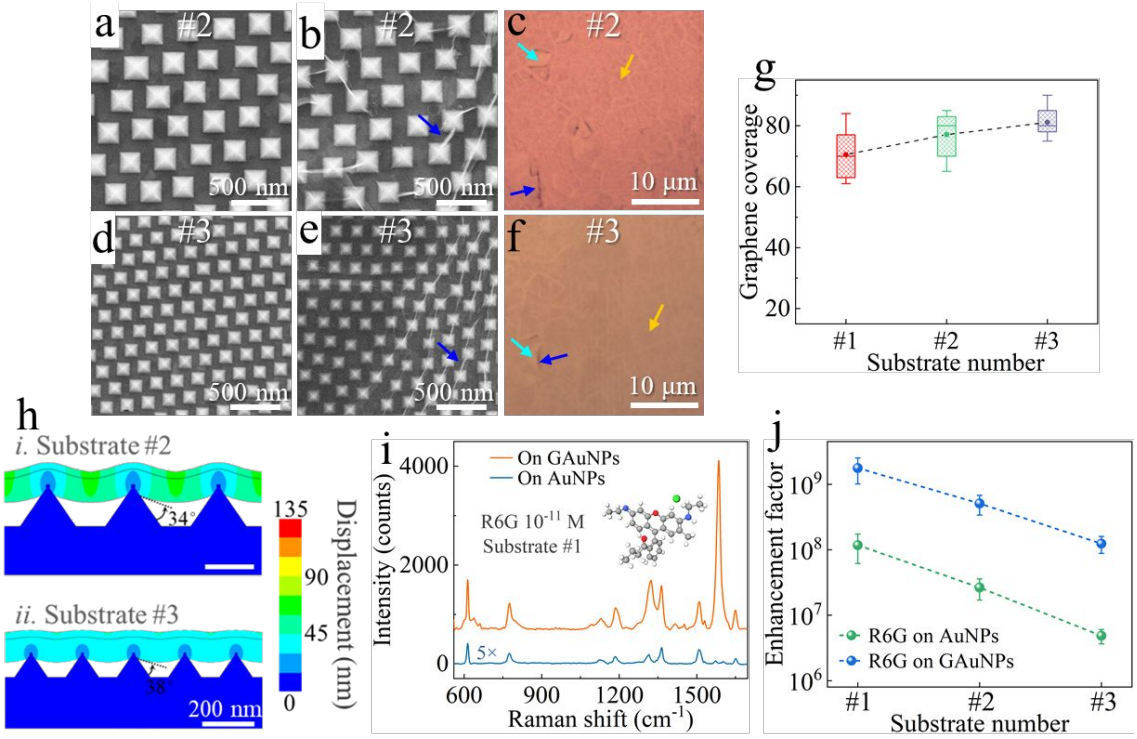

Figure 6. Morphology characterization of substrate #2, including SEM images (a) before and (b) after graphene transferred and (c) OM image with transferred graphene. Morphology characterization of substrate #3, including SEM images (d) before and (e) after graphene

393 transferred and (f) OM image with transferred graphene. Graphene monolayer is in orange arrow,
394 graphene wrinkle is in blue arrow, and bare AuNPs is in cyan arrow. (g) PMMA/paraffin-
395 transferred graphene coverage on the three types of substrates. (h) Finite element simulation
396 results of graphene transfer to the substrate (*i*) #2 and (*ii*) #3 using PMMA/paraffin. (i) The
397 surface-enhancement Raman spectroscopy of R6G on AuNPs and graphene-AuNPs (GAuNPs)
398 of substrate #1. (j) The analytical SERS enhancement factor of R6G on substrates with (on
399 GAuNPs) and without graphene (on AuNPs).

400 It is known that graphene-covered AuNPs could serve as a SERS platform for chemical and
401 biology sensing. Therefore, the SERS spectra of Rhodamine 6G (R6G) at a concentration of 10^{-11}
402 M (molar per liter; *ii*) on substrate #1 with and without graphene were collected and shown in
403 Figure 6i. It can be seen that R6G shows a series of Raman peaks in the range of 600-1600 cm^{-1},
404 the details of which were explained in SI Table S3. The AuNPs serve as a highly uniform and
405 sensitive SERS platform (orange curve), which is mainly based on the surface electromagnetic
406 field resonance enhancement mechanism caused by scattered light.[31] Besides the electromagnetic
407 mechanism, the GAuNP platform (blue curve) shows a higher SERS capability produced by the
408 chemical mechanism (CM) of graphene.[49] The average analytical SERS enhancement factors

409 (EFs) that come from graphene are ~20 times based on the CM enhancement, as shown in Figure
410 6j. The highest analytical EF of ~2 $\times$ 10^9 is obtained in GAuNP substrate #1. The detailed
411 calculation of EFs is shown in SI S6 and S7 parts.

412 ## 4. Conclusion

413 In conclusion, we report an effective large-area, clean, and high-coverage graphene transfer
414 method using PMMA/paraffin double layer to substrates with raised nanostructures, which can
415 also be applied to arbitrary substrates. The impact of supporting layers including PMMA,
416 paraffin and PMMA/paraffin on the transfer was studied in detail. High tensile strength and
417 young's modulus of PMMA facilitate the large-scale graphene transfer. The mechanical
418 properties and stable chemical property of paraffin lead to high coverage and clean graphene
419 transfer. PMMA/paraffin double-layer combines the advantages of the PMMA and paraffin
420 supporting layers, and achieves a large-area, high-coverage and high-quality graphene transfer to
421 AuNPs substrates. The electronic structure of the transferred graphene on AuNPs was examined
422 by analyzing the D peak in Raman spectra. The large curvature of graphene on AuNPs leads to
423 the polarization dependence of the D peak. Using a vector decomposition model to analyze the
424 Raman data, it was demonstrated that graphene on AuNPs shows tensile strain, which is caused

by the conformal fit of the graphene to the nanopyramids. It was also found that the higher nanopyramid density results in higher graphene coverage, which reaches 81% on the substrate with an AuNP density of 25 μm^{-2} (substrate #3). Graphene monolayer significantly enhanced the SERS effect of the AuNPs substrates, by increasing the analytical EF about ~20 times for R6G, and substrate #1 shows the highest analytical EF reaching ~2×10^9. Our results are of great interest for the transfer of large-area, clean and low-defect graphene onto arbitrary substrates, especially to those with raised micro-nano-structures, and thus of great potential for applications in the field of optoelectronics and SERS-based biosensing.

ASSOCIATED CONTENT

Supporting Information.

The following files are available free of charge.

Schematic illustration of the AuNPs substrate fabrication process; SEM characterizations of crucial steps of three types of substrates; The optimization of the O_2 plasma etching time; The shape characterizations of the nanopyramids; The paraffin wax thickness as a function of spin-

440 coating speed; The process of coverage statistics by Image J; The polarization independence of D
441 peak generated by defects of graphene; FDTD simulation results of the AuNP substrates; The
442 surface-enhancement Raman spectroscopy of graphene and R6G. (PDF)

443 AUTHOR INFORMATION

444 **Corresponding Author**

445 *Gang Niu - Electronic Materials Research Laboratory, Key Laboratory of the Ministry of
446 Education & International Center for Dielectric Research, School of Electronic Science and
447 Engineering, Xi'an Jiaotong University, Xi'an 710049, China; Email: gangniu@xjtu.edu.cn.
448 *Wei Ren - Electronic Materials Research Laboratory, Key Laboratory of the Ministry of
449 Education & International Center for Dielectric Research, School of Electronic Science and
450 Engineering, Xi'an Jiaotong University, Xi'an 710049, China; Email: wren@mail.xjtu.edu.cn.

451 **Author**

452 Heping Wu – Electronic Materials Research Laboratory, Key Laboratory of the Ministry of
453 Education & International Center for Dielectric Research, School of Electronic Science and
454 Engineering, Xi'an Jiaotong University, Xi'an 710049, China

455 Zhugen Yang - Cranfield Water Science Institute, School of Water, Energy and Environment,

456 Cranfield University, Cranfield, MK43 0AL, UK

457 Qihang Xu - Cranfield Water Science Institute, School of Water, Energy and Environment,

458 Cranfield University, Cranfield, MK43 0AL, UK

459 Liyan Dai – Electronic Materials Research Laboratory, Key Laboratory of the Ministry of

460 Education & International Center for Dielectric Research, School of Electronic Science and

461 Engineering, Xi'an Jiaotong University, Xi'an 710049, China

462 Luyue Jiang – Electronic Materials Research Laboratory, Key Laboratory of the Ministry of

463 Education & International Center for Dielectric Research, School of Electronic Science and

464 Engineering, Xi'an Jiaotong University, Xi'an 710049, China

465 Shijie Zhai – Electronic Materials Research Laboratory, Key Laboratory of the Ministry of

466 Education & International Center for Dielectric Research, School of Electronic Science and

467 Engineering, Xi'an Jiaotong University, Xi'an 710049, China

Jinyan Zhao – Electronic Materials Research Laboratory, Key Laboratory of the Ministry of Education & International Center for Dielectric Research, School of Electronic Science and Engineering, Xi'an Jiaotong University, Xi'an 710049, China

Nan Zhang – Electronic Materials Research Laboratory, Key Laboratory of the Ministry of Education & International Center for Dielectric Research, School of Electronic Science and Engineering, Xi'an Jiaotong University, Xi'an 710049, China

Gang Zhao - The college of Life Sciences and Medicine, Northwest University, No. 229 Taibai North Road, Xi'an, Shaanxi, 710069, P.R. China

Author Contributions

HPW, GN, and WR designed the work. HPW performed the experiments including the fabrication of different substrates, graphene transfer, characterizations, and data analysis. LYD and LYJ performed the AFM and SEM characterizations. HPW and GN wrote the manuscript and all the co-authors discussed the results and revised the manuscript.

Funding Sources

Key R&D Program of Shaanxi Province of China (2020GY-271).

The Fundamental Research Funds for the Central Universities(xjj2018016, xzd012020059).

The "111 Project" of China (B14040).

Notes

The authors declare no competing financial interest.

ACKNOWLEDGMENT

We acknowledge Mr. Zijun Ren, Mrs. Yu Wang and Mrs. Dan He at Instrument Analysis Center of Xi'an Jiaotong University for the assistance with SEM and Raman analysis.

REFERENCES

(1) Lee, S.; Lee, S. K.; Kang, C. G.; Cho, C.; Lee, Y. G.; Jung, U.;Lee, B. H. Graphene transfer in vacuum yielding a high quality graphene. *Carbon* **2015,** *93*, 286-294.

(2) Choi, W.; Lahiri, I.; Seelaboyina, R.;Kang, Y. S. Synthesis of Graphene and Its Applications: A Review. *Crit. Rev. Solid State Mater. Sci.* **2010,** *35* (1), 52-71.

(3) Kim, H.;Ahn, J.-H. Graphene for flexible and wearable device applications. *Carbon* **2017,** *120*, 244-257.

(4) Yu, Q.; Lian, J.; Siriponglert, S.; Li, H.; Chen, Y. P.;Pei, S.-S. Graphene segregated on Ni surfaces and transferred to insulators. *Appl. Phys. Lett.* **2008,** *93* (11).

(5) Li, X.; Cai, W.; An, J.; Kim, S.; Nah, J.; Yang, D.; Piner, R.; Velamakanni, A.; Jung, I.; Tutuc, E.; Banerjee, S. K.; Colombo, L.;Ruoff, R. S. Large-area synthesis of high-quality and uniform graphene films on copper foils. *Science* **2009,** *324* (5932), 1312-4.

(6) Muñoz, R.;Gómez-Aleixandre, C. Review of CVD Synthesis of Graphene. *Chem. Vap. Deposition* **2013,** *19* (10-11-12), 297-322.

(7) Khan, A.; Islam, S. M.; Ahmed, S.; Kumar, R. R.; Habib, M. R.; Huang, K.; Hu, M.; Yu, X.;Yang, D. Direct CVD Growth of Graphene on Technologically Important Dielectric and Semiconducting Substrates. *Adv. Sci.* **2018,** *5* (11), 1800050.

(8) Bae, S.; Kim, H.; Lee, Y.; Xu, X.; Park, J. S.; Zheng, Y.; Balakrishnan, J.; Lei, T.; Kim, H. R.; Song, Y. I.; Kim, Y. J.; Kim, K. S.; Ozyilmaz, B.; Ahn, J. H.; Hong, B. H.;Iijima, S. Roll-to-roll production of 30-inch graphene films for transparent electrodes. *Nat. Nanotechnol.* **2010,** *5* (8), 574-8.

(9) Luo, Z.; Lu, Y.; Singer, D. W.; Berck, M. E.; Somers, L. A.; Goldsmith, B. R.;Johnson, A. T. C. Effect of Substrate Roughness and Feedstock Concentration on Growth of Wafer-Scale Graphene at Atmospheric Pressure. *Chem. Mater.* **2011,** *23* (6), 1441-1447.

(10) Robertson, A. W.;Warner, J. H. Hexagonal single crystal domains of few-layer graphene on copper foils. *Nano Lett.* **2011,** *11* (3), 1182-9.

(11) Yang, G.; Li, L.; Lee, W. B.;Ng, M. C. Structure of graphene and its disorders: a review. *Sci. Technol. Adv. Mater.* **2018,** *19* (1), 613-648.

(12) Meyer, J. C.; Geim, A. K.; Katsnelson, M. I.; Novoselov, K. S.; Booth, T. J.;Roth, S. The structure of suspended graphene sheets. *Nature* **2007,** *446* (7131), 60-3.

(13) Chen, M.; Haddon, R. C.; Yan, R.;Bekyarova, E. Advances in transferring chemical vapour deposition graphene: a review. *Mater. Horizons* **2017,** *4* (6), 1054-1063.

(14) Leong, W. S.; Wang, H.; Yeo, J.; Martin-Martinez, F. J.; Zubair, A.; Shen, P. C.; Mao, Y.; Palacios, T.; Buehler, M. J.; Hong, J. Y.;Kong, J. Paraffin-enabled graphene transfer. *Nat. Commun.* **2019,** *10* (1), 867.

(15) Borin Barin, G.; Song, Y.; de Fátima Gimenez, I.; Souza Filho, A. G.; Barreto, L. S.;Kong, J. Optimized graphene transfer: Influence of polymethylmethacrylate (PMMA) layer concentration and baking time on graphene final performance. *Carbon* **2015,** *84*, 82-90.

(16) Zhang, D.; Jin, Z.; Shi, J.; Wang, X.; Peng, S.;Wang, S. The electrochemical transfer of CVD-graphene using agarose gel as solid electrolyte and mechanical support layer. *Chem. Commun.* **2015,** *51* (14), 2987-90.

(17) Pantano, M. F.; Iacob, E.; Picciotto, A.; Margesin, B.; Centeno, A.; Zurutuza, A.; Galiotis, C.; Pugno, N. M.;Speranza, G. Investigation of charges-driven interactions between graphene and different SiO2 surfaces. *Carbon* **2019,** *148*, 336-343.

(18) Fan, X. F.; Zheng, W. T.; Chihaia, V.; Shen, Z. X.;Kuo, J. L. Interaction between graphene and the surface of SiO2. *J. Phys.: Condens. Matter* **2012,** *24* (30), 305004.

(19) Wang, P.; Xia, M.; Liang, O.; Sun, K.; Cipriano, A. F.; Schroeder, T.; Liu, H.;Xie, Y.-H. Label-free SERS selective detection of dopamine and serotonin using graphene-Au nanopyramid heterostructure. *Anal. Chem.* **2015,** *87* (20), 10255-10261.

(20) Jiang, L.; Niu, G.; Wu, H.; Zhao, J.; Liu, Y.; Xie, Z.; Yao, Q.; Yu, W.; Ren, W.;Zhao, G. Detection of K562 Leukemia Cells in Different States Using a Graphene-SERS Platform. *ACS Appl. Nano Mater.* **2021,** *4* (9), 8972-8978.

(21) Wang, Y.; Zhang, S.; Chen, H.; Li, H.; Zhang, P.; Zhang, Z.; Liang, G.;Kong, J. One-pot facile decoration of graphene nanosheets with Ag nanoparticles for electrochemical oxidation of methanol in alkaline solution. *Electrochem. Commun.* **2012,** *17*, 63-66.

(22) Tae Lim, J.; Lee, H.; Cho, H.; Kwon, B. H.; Sung Cho, N.; Kuk Lee, B.; Park, J.; Kim, J.; Han, J. H.; Yang, J. H.; Yu, B. G.; Hwang, C. S.; Chu Lim, S.;Lee, J. I. Flexion bonding transfer of multilayered graphene as a top electrode in transparent organic light-emitting diodes. *Sci Rep* **2015,** *5*, 17748.

(23) Gong, F.; Wang, H.;Wang, Z. S. Self-assembled monolayer of graphene/Pt as counter electrode for efficient dye-sensitized solar cell. *Phys. Chem. Chem. Phys.* **2011,** *13* (39), 17676-82.

(24) Xu, G.; Liu, J.; Wang, Q.; Hui, R.; Chen, Z.; Maroni, V. A.;Wu, J. Plasmonic graphene transparent conductors. *Adv. Mater.* **2012,** *24* (10), OP71-6.

(25) Tan, C.; Huang, X.;Zhang, H. Synthesis and applications of graphene-based noble metal nanostructures. *Mater. Today* **2013,** *16* (1-2), 29-36.

(26) Wu, H.; Niu, G.; Ren, W.; Jiang, L.; Zhao, J.; Quan, Y.; Ren, M. X.; Yu, W.; Zhang, Y.; Cao, X.; Liu, Y.; An, R.; Dai, L.; Wang, Z.; Zhao, L.; Xie, Z.;Zhao, G. Highly sensitive label-free detection of analytes at different scales using uniform graphene-nanopyramids hybrid SERS system. *Sens. Actuator B Chem.* **2022,** *354*.

(27) Wu, H.; Niu, G.; Ren, W.; Jiang, L.; Liang, O.; Zhao, J.; Liu, Y.;Xie, Y. H. Crucial impact of hydrophilicity on the self-assemble 2D colloidal crystals using Langmuir-Blodgett method. *Langmuir* **2020,** *36* (34), 10061-10068.

(28) Ye, S.; Huang, H.; Yuan, C.; Liu, F.; Zhai, M.; Shi, X.; Qi, C.;Wang, G. Thickness-Dependent Strain Effect on the Deformation of the Graphene-Encapsulated Au Nanoparticles. *J. Nanomater.* **2014,** *2014*, 1-6.

(29) Fechine, G. J. M.; Martin-Fernandez, I.; Yiapanis, G.; Bentini, R.; Kulkarni, E. S.; Bof de Oliveira, R. V.; Hu, X.; Yarovsky, I.; Castro Neto, A. H.;Özyilmaz, B. Direct dry transfer of chemical vapor deposition graphene to polymeric substrates. *Carbon* **2015,** *83*, 224-231.

(30) Hong, S. K.; Song, S. M.; Sul, O.;Choz, B. J. Carboxylic Group as the Origin of Electrical Performance Degradation during the Transfer Process of CVD Growth Graphene. *Journal of the Electrochemical Society* **2012,** *159* (4), K107-K109.

(31) Zong, C.; Xu, M.; Xu, L. J.; Wei, T.; Ma, X.; Zheng, X. S.; Hu, R.;Ren, B. Surface-Enhanced Raman Spectroscopy for Bioanalysis: Reliability and Challenges. *Chem. Rev.* **2018,** *118* (10), 4946-4980.

(32) Casiraghi, C.; Hartschuh, A.; Qian, H.; Piscanec, S.; Georgi, C.; Fasoli, A.; Novoselov, K. S.; Basko, D. M.;Ferrari, A. C. Raman spectroscopy of graphene edges. *Nano Lett.* **2009,** *9* (4), 1433-41.

(33) Abdel-Wahab, A. A.; Ataya, S.;Silberschmidt, V. V. Temperature-dependent mechanical behaviour of PMMA: Experimental analysis and modelling. *Polym. Test.* **2017,** *58*, 86-95.

(34) Toossi, A.; Moghadas, H.; Daneshmand, M.;Sameoto, D. Bonding PMMA microfluidics using commercial microwave ovens. *J. Micromech. Microeng.* **2015,** *25* (8).

(35) DeSain, J.; Brady, B.; Metzler, K.; Curtiss, T.;Albright, T. Tensile Tests of Paraffin Wax for Hybrid Rocket Fuel Grains. In *45th AIAA/ASME/SAE/ASEE Joint Propulsion Conference & Exhibit*, 2009.

(36) Mann, A.; Bürgel, C.;Groche, P. A Modeling Strategy for Predicting the Properties of Paraffin Wax Actuators. *Actuators* **2018,** *7* (4).

(37) Li, C.; Liu, Q. W.; Peng, X. B.;Fan, S. C. Measurement of thermal expansion coefficient of graphene diaphragm using optical fiber Fabry-Perot interference. *Meas. Sci. Technol.* **2016,** *27* (7).

(38) Li, Q. Y.; Xia, K.; Zhang, J.; Zhang, Y.; Li, Q.; Takahashi, K.;Zhang, X. Measurement of specific heat and thermal conductivity of supported and suspended graphene by a comprehensive Raman optothermal method. *Nanoscale* **2017,** *9* (30), 10784-10793.

(39) Zhu, S. E.; Shabani, R.; Rho, J.; Kim, Y.; Hong, B. H.; Ahn, J. H.;Cho, H. J. Graphene-based bimorph microactuators. *Nano Lett.* **2011,** *11* (3), 977-81.

(40) Magouh, N.; Dietze, M.; Bakhti, H.; Solterbeck, C.-H.; Azrar, L.;Es-Souni, M. Finite element analysis and EMA predictions of the dielectric and pyroelectric properties of 0-3 Pz59/PVDF-TrFE composites with experimental validation. *Sens. Actuator A Phys.* **2020,** *310*.

(41) Gupta, A. K.; Nisoli, C.; Lammert, P. E.; Crespi, V. H.;Eklund, P. C. Curvature-induced D-band Raman scattering in folded graphene. *J. Phys.: Condens. Matter* **2010,** *22* (33), 334205.

(42) Gupta, A. K.; Russin, T. J.; Gutierrez, H. R.;Eklund, P. C. Probing graphene edges via Raman scattering. *ACS Nano* **2009,** *3* (1), 45-52.

(43) Wang, P.; Zhang, W.; Liang, O.; Pantoja, M.; Katzer, J.; Schroeder, T.;Xie, Y. H. Giant optical response from graphene--plasmonic system. *ACS Nano* **2012,** *6* (7), 6244-9.

(44) Neumann, C.; Reichardt, S.; Venezuela, P.; Drogeler, M.; Banszerus, L.; Schmitz, M.; Watanabe, K.; Taniguchi, T.; Mauri, F.; Beschoten, B.; Rotkin, S. V.;Stampfer, C. Raman spectroscopy as probe of nanometre-scale strain variations in graphene. *Nat. Commun.* **2015,** *6*, 8429.

(45) Lee, J. E.; Ahn, G.; Shim, J.; Lee, Y. S.;Ryu, S. Optical separation of mechanical strain from charge doping in graphene. *Nat. Commun.* **2012,** *3*, 1024.

(46) Banszerus, L.; Janssen, H.; Otto, M.; Epping, A.; Taniguchi, T.; Watanabe, K.; Beschoten, B.; Neumaier, D.;Stampfer, C. Identifying suitable substrates for high-quality graphene-based heterostructures. *2D Mater.* **2017,** *4* (2).

(47) Song, Y.; Liu, J.; Quan, L.; Pan, N.; Zhu, H.;Wang, X. Size Dependence of Compressive Strain in Graphene Flakes Directly Grown on SiO2/Si Substrate. *J. Phys. Chem. C* **2014,** *118* (23), 12526-12531.

(48) Zhao, Y.; Liu, X.; Lei, D. Y.;Chai, Y. Effects of surface roughness of Ag thin films on surface-enhanced Raman spectroscopy of graphene: spatial nonlocality and physisorption strain. *Nanoscale* **2014,** *6* (3), 1311-7.

(49) Xu, W.; Mao, N.;Zhang, J. Graphene: a platform for surface-enhanced Raman spectroscopy. *Small* **2013,** *9* (8), 1206-24.

Cranfield University

CERES Research Repository **https://dspace.lib.cranfield.ac.uk/**

School of Water, Energy and Environment (SWEE) Staff publications (SWEE)

Large-area and clean graphene transfer on gold-nanopyramid-structured substrates: implications for surface-enhanced Raman scattering detection

Wu, Heping

2022-03-16

Attribution-NonCommercial 4.0 International

Wu H, Niu G, Ren W, et al., (2022) Large-area and clean graphene transfer on gold-nanopyramid-structured substrates: implications for surface-enhanced Raman scattering detection, ACS Applied Nano Materials, Volume 5, Issue 3, March 2022, pp. 3878-3888
https://doi.org/10.1021/acsanm.1c04491

Downloaded from CERES Research Repository, Cranfield University